Asian Journal of Chemistry; Vol. 37, No. 3 (2025), 609-616

ASIAN JOURNAL OF CHEMISTRY

https://doi.org/10.14233/ajchem.2025.33257

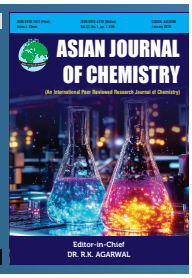

Structural, Magnetic and Antimicrobial Performance of Hydrothermally Synthesized Mg-Zn Ferrite Nanoparticles

G. Ameer Basha[1], C.V. Krishna Reddy[2], Lingala Eswaraditya Reddy[3], Gaurav Mahnot Jain[3], Dhruv Gollapudi[3], I. Balakrishna[3] and Gubbala V. Ramesh[4,*]

[1]Department of Physics, Silver Jubilee Government College, Kurnool-518002, India
[2]Department of Physics, Rayalaseema University, Kurnool-518002, India
[3]Department of Chemical Engineering, Chaitanya Bharathi Institute of Technology, Kokapet, Gandipet, Hyderabad-500075, India
[4]Department of Chemistry, Chaitanya Bharathi Institute of Technology, Kokapet, Gandipet, Hyderabad-500075, India

*Corresponding author: E-mail: venkataramesh_chm@cbit.ac.in

Received: 24 December 2024; *Accepted*: 1 February 2025; *Published online*: 28 February 2025; AJC-21917

This study investigated the structural, magnetic and antibacterial properties of magnesium-zinc ferrite (Mg-Zn ferrite) nanoparticles, which were synthesized through hydrothermal method. The analysis revealed that the lattice parameters and crystallite sizes diminished as zinc content increased, showing a reduction from 36.6 nm for $MgFe_2O_4$ to 22.17 nm for $ZnFe_2FeO_4$, as determined through X-ray diffraction (XRD). An increased level of Zn substitution led to greater lattice strain and enhanced cation exchange, as evidenced by Raman spectrum. Magnetic studies revealed that the ideal cation configuration was $Mg_{0.5}Zn_{0.5}Fe_2O_4$, with a peak saturation magnetization of 28.53 emu/g. The antibacterial results showed that the zinc-rich samples were efficient against both *Candida albicans* and Gram-positive bacteria, specifically *Staphylococcus aureus*. This phenomenon was linked to an increase in reactive oxygen species (ROS) production and the liberation of Zn^{2+} ions into the adjacent environment.

Keywords: $MgFe_2O_4$, $ZnFe_2O_4$, Spinel ferrites, Magnetic properties, Antibacterial activity.

INTRODUCTION

Ferrite nanoparticles, particularly those with a spinel structure (MFe_2O_4), have become an increasingly prevalent topic due to their unique magnetic properties and extensive industrial applications [1]. Ferrimagnetism is a property of these materials that occurs when a net magnetic moment is produced by atoms on separate sublattices, which are opposite to one another. Their exceptional quality renders them useful in a wide range of fields, including as environmental cleanup, biological imaging and magnetic storage systems [2].

Metal cations fill the interstitial tetrahedral (A) and octahedral (B) spaces in the spinel ferrite structure, which is a cubic lattice of oxygen ions face-centered. The electrical and magnetic characteristics of the material are strongly affected by the disposition of these cations relative to the A and B sites. As an example, in typical spinel's, the tetrahedral sites are occupied by divalent cations and the octahedral sites by trivalent cations. Inverse spinel's, on the other hand, only octahedral sites contain divalent cations, whereas tetrahedral sites have trivalent cations. The total magnetic behaviour of the ferrite nanoparticles is strongly affected by this cation distribution [3,4].

Nanoscale particles have a high surface-to-volume ratio, making them more chemically reactive and distinct magnetic properties than bulk particles. This size-dependent behaviour is critical for nanoparticle-biosystem interactions in targeted medication delivery and MRI [5]. In addition, ferrite nanoparticles may be fine-tuned in size, shape and composition to suit specific applications. The extensive usage of spinel ferrite nanoparticles in cutting-edge technological applications is based on their unique magnetic and structural characteristics. To maximize their performance in different domains, one must comprehend the relation between their crystal structure, distribution of cations and consequent magnetic behaviour [6]. The structural and functional features of spinel ferrites are greatly affected by their synthesis technique, which is responsible for their tunable

qualities [7]. The capacity to create nanoparticles with uniform morphology, good crystallinity and fine size control at very low temperatures makes the hydrothermal approach stand out among alternative synthesis processes [8]. This technique ensures phase homogeneity and purity through the utilization of water-based metal salt solutions in a regulated environment of temperature and pressure.

Magnesium-zinc ferrites ($Mg_xZn_{1=x}Fe_2O_4$) have garnered considerable interest among the several types of spinel ferrites due to their adjustable magnetic characteristics, The saturation magnetization, coercivity and other parameters can be tuned by adjusting the magnesium-to-zinc ratio. Mg-Zn ferrites are used in electromagnetic interference suppression and high-frequency transformer cores because to their tunability. They are appropriate for these tasks due to their high electrical resistance and low eddy current losses [9]. Nanoparticles made of spinel ferrite have also gained interest due to their antibacterial capabilities in recent years. Due to their ability to generate reactive oxygen species (ROS), which, in some environments, can degrade bacterial cell walls, they show promise as antimicrobials. Considerations including composition, size and surface functionalization determine the efficacy of these nanoparticles. With antibiotic resistance on the rise, it is more important than ever to study these characteristics in order to develop new antibacterial medicines [10,11].

In this work, hydrothermal technique approach was used to synthesize Mg-Zn ferrite nanoparticles and then characterized for their structural and magnetical properties. Furthermore, in order to investigate their possible biological uses, the antibacterial effectiveness of these nanoparticles tested against common bacterial strains.

EXPERIMENTAL

In this work, ferric nitrate nonahydrate ($Fe(NO_3)_3·9H_2O$), supplied by Research-Lab Fine Chem Industries, India. Zinc acetate dihydrate ($Zn(CH_3COO)_2·2H_2O$), magnesium chloride hexahydrate ($MgCl_2·6H_2O$) and citric acid monohydrate were supplied by SDFCL Chemicals, India. Ethanol was supplied by CHFC Co., China and distilled water was used throughout the experiments.

Synthesis of spinel ferrites nanoparticles: The spinel ferrites were synthesized by a hydrothermal technique employing stoichiometric quantities of precursor materials. Precisely, $Zn(CH_3COO)_2·2H_2O$ (0.02 mol) and $Fe(NO_3)_3·9H_2O$ (0.04 mol) were solubilized in a aqueous citric acid monohydrate (16.26 g) solution. For other ferrites, the iron precursor was maintained at 0.04 mol while the ratios of zinc and magnesium precursors were varied. The total solution volume was adjusted to 60 mL with distilled water. The solution was thoroughly agitated and thereafter put into Teflon-lined stainless-steel autoclaves. The autoclaves underwent a hydrothermal reaction at 150 ºC for 16 h under continuous heating conditions. Upon completion of the reaction, the autoclave was cool down to ambient temperature. The resultant precipitate was washed multiple times with water and subsequently with ethanol to eliminate any remaining ions. The cleaned product was centrifuged and dried at 120 ºC for 1 h. The dry powder was subjected to annealed at 600 ºC for 4 h to enhance crystallinity.

Characterization: The powder XRD patterns were recorded using a Bruker D8 Advance diffractometer operating at 40 kV and 40 mA with Cu*K*α radiation (λ = 1.5406 Å). Data were collected over a 2θ range of 10-80º. Zeta potential measurements were performed using a nanoplus zeta/nanoparticle analyzer (Particulate Systems). Samples were dispersed in distilled water and analyzed at 27 ºC, with each measurement averaged over 3 runs to ensure accuracy. Morphological and elemental analyses were conducted using an FEI Quanta FEG 250 FESEM equipped with an Ametek EDX detector. The magnetic properties were characterized using a Quantum Design Physical Property Measurement System (PPMS Evercool-II), which operates as a cryogen-free platform utilizing a GM Cryocooler. The system provides precise measurements across a wide temperature range of 3-370 K and under magnetic fields up to 9 Tesla. Magnetization measurements were performed using the vibrating sample magnetometer (VSM) option.

A**ntibacterial activity:** The antimicrobial activity was evaluated using culture of Gram-positive bacteria (*Staphylococcus aureus*) and fungal culture (*Candida albicans*), with standard antibiotics streptomycin (5 µg/mL) and fluconazole (5 µg/mL) as control [12]. Nutrient agar media, potato dextrose agar media and yeast extract peptone media were used for bacterial and fungal growth, along with sterile petri plates and a bacterial incubator. Active bacterial cultures were prepared by transferring a single bacterial colony from a pure culture into a 150 mL conical flask containing 50 mL of nutrient broth media, followed by incubation at 37 ºC for 8-12 h. For sample preparation, compounds were dissolved in appropriate solvents such as water, methanol or DMSO to prepare aliquots of varying concentrations for minimum inhibitory concentration (MIC) assays, while liquid samples were directly diluted as required. The antibacterial assay was performed using the pour plate method, where 1% of bacterial cultures were mixed with autoclaved agar media at near-solidifying temperature, poured into plates and allowed to solidify. Wells were then made using a sterile well borer and 100 µL of each sample was loaded into the wells. Plates were incubated at 37 ºC for 18-24 h in a bacterial incubator and the zone of inhibition around the wells was observed and recorded to evaluate the antibacterial activity.

RESULTS AND DISCUSSION

XRD studies: There were substantial insights into the crystallographic characteristics of Mg-Zn ferrite samples analyzed structurally, regardless of their composition. The cubic spinel structure was validated by X-ray diffraction (XRD) patterns for all samples. The significant (311) peak showed consistent changes in 2θ values (Fig. 1) [13,14]. The 2θ values shifted slightly towards higher angles as the Zn concentration increased, suggesting that the lattice contracted because the ionic radius of Zn^{2+} was bigger than that of Mg^{2+}. Zn^{2+} ions redistribute themselves throughout the lattice and preferentially occupy tetrahedral (A) sites, according to Vegard's rule, which explains this behaviour [15,16]. From 36.6 nm for $MgFe_2O_4$ to 22.17 nm

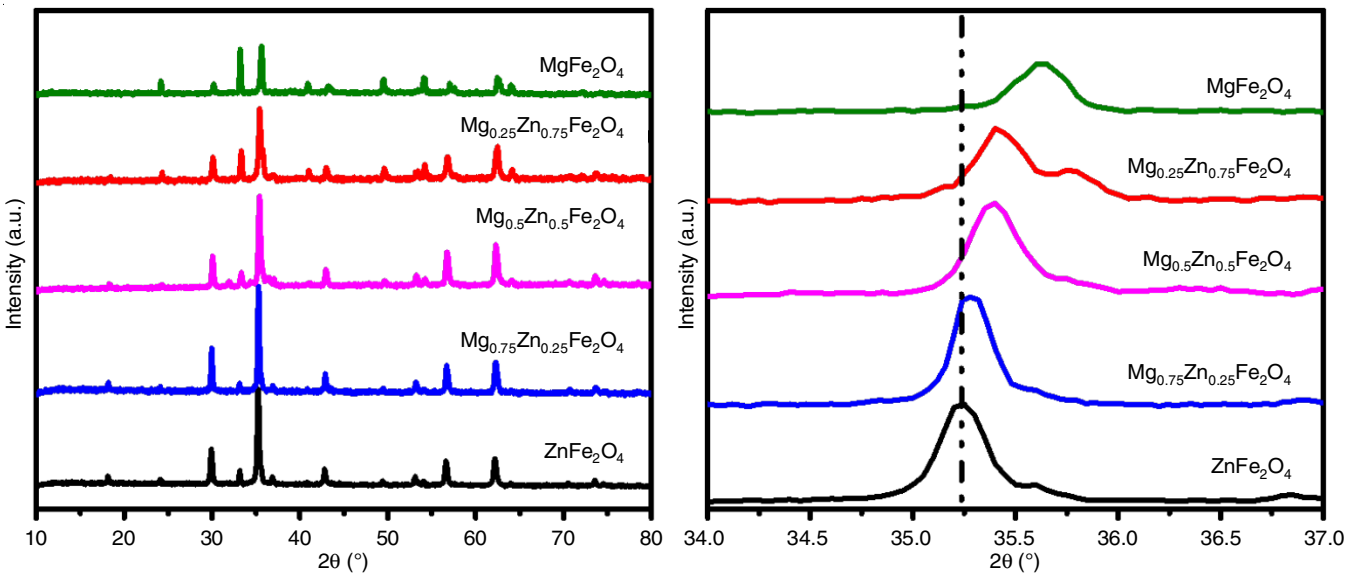

Fig. 1. X-ray diffraction (XRD) patterns of Mg-Zn ferrite nanoparticles with varying compositions: $MgFe_2O_4$, $Zn_{0.25}Mg_{0.75}Fe_2O_4$, $Zn_{0.5}Mg_{0.5}Fe_2O_4$, $Zn_{0.75}Mg_{0.25}Fe_2O_4$ and $ZnFe_2O_4$. The left panel shows the full XRD profiles, confirming the cubic spinel structure with prominent peaks indexed to (311), (400) and (440) planes. The right panel zooms into the (311) diffraction peak in the 2θ range of 34°-37°, highlighting systematic shifts toward higher angles with increasing Zn content, indicating lattice contraction due to Zn substitution

for $ZnFe_2O_4$, the crystallite size decreased as the Zn content increased, indicating an increase in lattice strain and disorder. Consistent with other investigations, this trend in crystallite size highlights the synthesis process's repeatability.

A tendency towards lower values for the lattice parameter and unit cell volume was seen as the Zn concentration increased, providing more evidence of lattice contraction. The larger molecular weight of Zn compared to Mg caused the theoretical density (ρx) to rise following Zn substitution. As a result of cation redistribution's effect on the crystal structure, hopping lengths for both tetrahedral (A) and octahedral (B) sites changed consistently with composition. Due to these structural modifications, Zn-rich samples may exhibit enhanced stability and possess specific functional attributes that render them advantageous in domains such as photocatalysis and magnetism. Table-1 presents a summary of the structural properties obtained from the XRD analysis.

TABLE-1
XRD DATA OF Mg-Zn FERRITE NANOPARTICLES

Sample composition	Lattice parameter (Å)	Crystallite size (nm)	Theoretical density (g/cm^3)	Unit cell volume (Å^3)
$MgFe_2O_4$	8.3712	36.60	4.5306	586.60
$Mg_{0.75}Zn_{0.25}Fe_2O_4$	8.4330	27.45	5.3060	599.72
$Mg_{0.5}Zn_{0.5}Fe_2O_4$	8.4250	25.75	5.1030	598.01
$Mg_{0.25}Zn_{0.75}Fe_2O_4$	8.4150	23.84	4.9250	595.88
$ZnFe_2O_4$	8.4050	22.17	4.7470	593.76

Raman spectral studies: The structural features and vibrational modes of $MgFe_2O_4$, $Mg_{0.75}Zn_{0.25}Fe_2O_4$, $Mg_{0.5}Zn_{0.5}Fe_2O_4$, $Mg_{0.25}Zn_{0.75}Fe_2O_4$ and $ZnFe_2O_4$ were studied using Raman spectroscopy and are presented in Fig. 2. Typical active modes seen in ferrites, such as A_{1g}, E_g and $3F_{2g}$, were confirmed by Raman spectrum, which matched to the spinel structure [17]. The symmetric stretching vibrations of oxygen ions with metal cations in the tetrahedral sites are responsible for the prominent peaks at 680 cm^{-1}, whereas the asymmetric vibrations in the octahedral sites give rise to the peaks near 480 cm^{-1}. It is significant that as the Zn concentration increased, the Raman modes shifted to higher wavenumbers and exhibited broader peaks, signifying greater structural disorder and enhanced cation inversion at the tetrahedral and octahedral sites. These results are consistent with earlier research that found strain effects and cation redistribution in Mg ferrites doped with Zn [18].

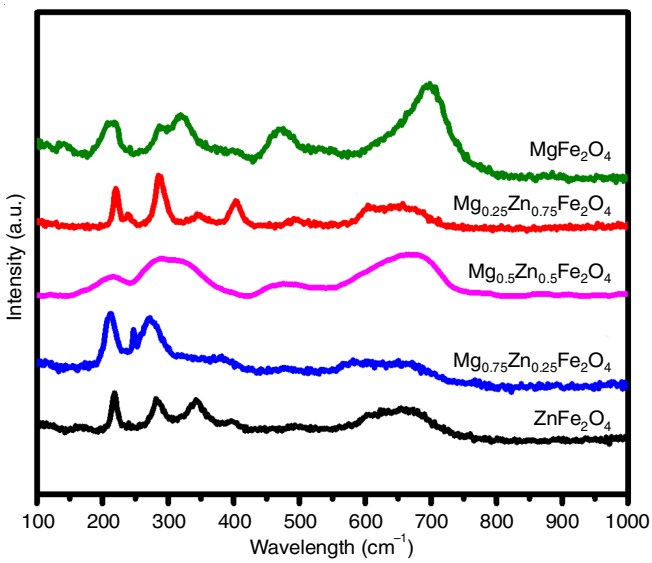

Fig. 2. Raman spectra of Mg-Zn ferrite nanoparticles with varying compositions: $MgFe_2O_4$, $Zn_{0.25}Mg_{0.75}Fe_2O_4$, $Zn_{0.5}Mg_{0.5}Fe_2O_4$, $Zn_{0.75}Mg_{0.25}Fe_2O_4$ and $ZnFe_2O_4$, showing characteristic vibrational modes of the spinel structure

The Zn substitution results in a reduction of particle size and alters the vibrational dynamics, evidenced by the broadening of the Raman spectra and the shifting of the peaks. Sharper and more clearly defined peaks were observed in the Mg-rich samples, including $MgFe_2O_4$, which may be attributed to their greater crystallinity and more organized lattice structures. The wider peaks observed in Zn-rich materials, like $ZnFe_2O_4$, could be a result of higher lattice strain and more inversion degrees. Earlier findings that increasing Zn concentration causes local structural distortions that impact the spinel lattice's vibrational characteristics and functional behaviour are supported by this trend [19].

These results are supported by related Raman studies on ferrites, which demonstrate that the Raman-active modes are affected by cation distribution and lattice disorder. The Raman-active modes and their features are summarized in Table-2, which provides a thorough comparison of vibrational properties with regard to cation substitution and structural integrity across all of the compositions that were investigated. The complex relationship between vibrational dynamics and cation distribution in Mg-Zn ferrites is brought to light by these results. The spectrum characteristics and Raman shifts that have been found give light on the effects of Zn substitution on the structural and vibrational properties of these ferrites, which in turn help to explain their practical uses in areas including biomedical imaging, magnetism and catalysis [20].

Morphological studies: Fig. 3 shows SEM micrographs of Mg-Zn ferrite nanoparticles ($MgFe_2O_4$, $Zn_{0.25}Mg_{0.75}Fe_2O_4$, $Zn_{0.5}Mg_{0.5}Fe_2O_4$, $Zn_{0.75}Mg_{0.25}Fe_2O_4$ and $ZnFe_2O_4$) exhibit nanocrystalline structures characterized by spherical agglomerates. In magnesium-rich compositions (*e.g.* $MgFe_2O_4$), the particles demonstrate more compact and densely packed agglomerates. This trend is due to magnesium ions' propensity to enhance grain development and diminish porosity during synthesis. With the rise in Zn concentration, the agglomerates exhibit a more loosely packed arrangement, with the $ZnFe_2O_4$ sample demonstrating a more porous and open structure. The change to a porous structure in Zn-rich samples may result from the substitution of Mg^{2+} with Zn^{2+}, which modifies the growth kinetics and diminishes the particle-particle interactions. The reduction in compactness corresponds with the diminished polarizability of Zn^{2+} ions, as documented in the literature.

TABLE-2
RAMAN SPECTRAL DATA OF Mg-Zn FERRITE NANOPARTICLES WITH VARYING COMPOSITIONS

Sample composition	Peak position (cm^{-1})	Bandwidth (cm^{-1})	Interpretation
$MgFe_2O_4$	680, 480	Sharp	High crystallinity, minimal inversion
$Mg_{0.75}Zn_{0.25}Fe_2O_4$	682, 482	Slightly broad	Moderate inversion and lattice strain
$Mg_{0.5}Zn_{0.5}Fe_2O_4$	685, 485	Broad	Increased structural disorder
$Mg_{0.25}Zn_{0.75}Fe_2O_4$	687, 487	Broader	Higher inversion and significant lattice strain
$ZnFe_2O_4$	690, 490	Broadest	Maximum inversion and lattice distortion

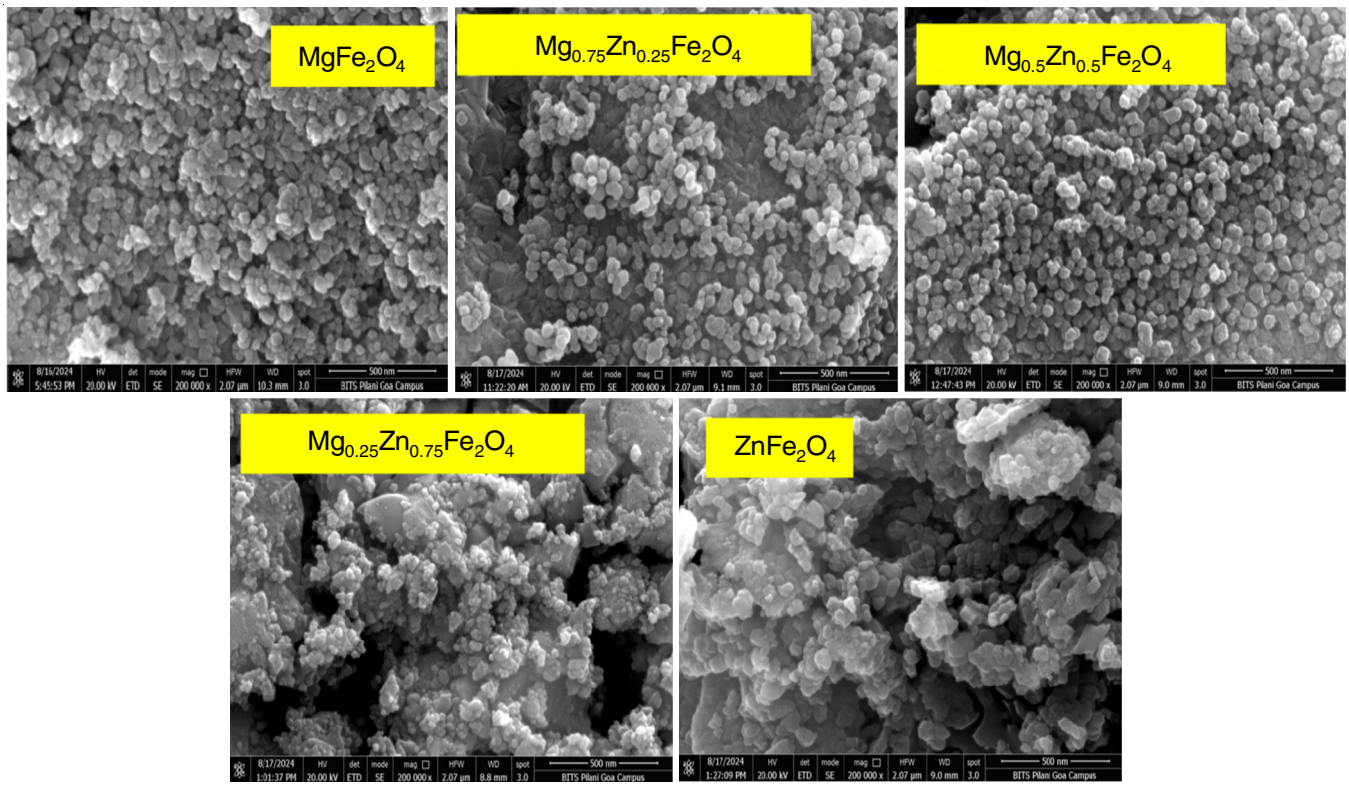

Fig. 3. SEM micrographs of Mg-Zn ferrite nanoparticles with compositions $MgFe_2O_4$, $Zn_{0.25}Mg_{0.75}Fe_2O_4$, $Zn_{0.5}Mg_{0.5}Fe_2O_4$, $Zn_{0.75}Mg_{0.25}Fe_2O_4$ and $ZnFe_2O_4$

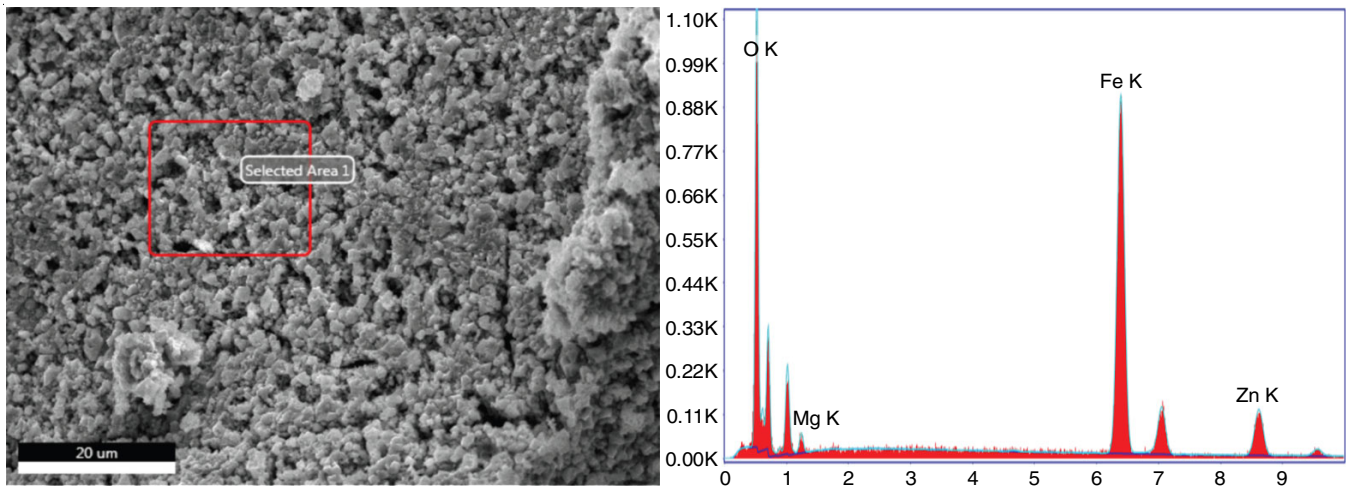

Fig. 4. EDAX analysis of $Zn_{0.5}Mg_{0.5}Fe_2O_4$ showing elemental peaks for Fe, Zn, Mg and O, confirming the composition and purity of sample without detectable impurities

The images obtained from the SEM reveal uniform particle size distributions across all compositions, with differences in agglomeration linked to variations in cation distribution. Such agglomerations are characteristic of the spinel ferrites produced *via* hydrothermal techniques and aligned with their magnetic properties, which promote interparticle magnetic interactions. These results provide substantial insights into the relationship between composition and morphology in Mg-Zn ferrites, highlighting the impact of cation substitution on the structural characteristics of the nanoparticles. Crystallite size determined by XRD results agreed well with the average particle size derived from SEM pictures.

The data show that when the zinc content increases, the particle size consistently decreases. Particle size for $MgFe_2O_4$ is around 50 nm and for $ZnFe_2O_4$ are about 38 nm. The continuous substitution of magnesium with zinc results in smaller particles since zinc influences growth and nucleation processes associated with synthesis. Zinc ions inhibit the aggregation of particles, facilitating the formation of smaller particles [21].

The EDAX spectrum for $Zn_{0.5}Mg_{0.5}Fe_2O_4$ shows prominent peaks corresponding to Fe, Zn, Mg and O, confirming the presence of expected elements in the sample (Fig. 4). No additional peaks are observed, indicating the high purity of the synthesized material.

Magnetic studies: The room temperature magnetization (M-H) tests were used to evaluate the magnetic characteristics of the synthesized Mg-Zn ferrite samples. Saturation magnetization (M_s) values showed substantial composition-dependent variation in sample magnetic behaviour, suggesting a considerable dependency on cation distribution inside the spinel lattice (Table-3). At 28.53 emu/g, $Mg_{0.5}Zn_{0.5}Fe_2O_4$ had the greatest Ms, indicating that the magnetic interactions were improved due to the best arrangement of the cations (Fig. 5). On the other hand, $Mg_{0.75}Zn_{0.25}Fe_2O_4$ had the lowest Ms value of 4.07 emu/g. This might be due to the substitution of Zn for Mg broke the magnetic order. Following a similar pattern, the remanent magnetization (M_r) was also very high for $Mg_{0.5}Zn_{0.5}Fe_2O_4$, at

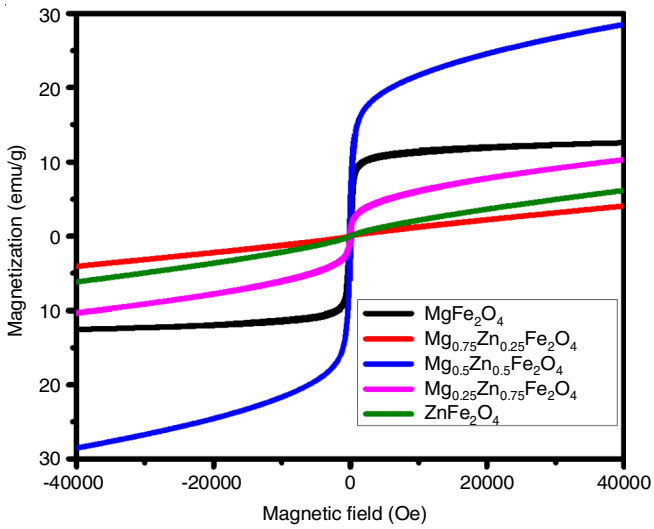

Fig. 5. Magnetization (M-H) curves of Mg-Zn ferrite nanoparticles with compositions $MgFe_2O_4$, $Zn_{0.25}Mg_{0.75}Fe_2O_4$, $Zn_{0.5}Mg_{0.5}Fe_2O_4$, $Zn_{0.75}Mg_{0.25}Fe_2O_4$ and $ZnFe_2O_4$ measured at room temperature, showing composition-dependent magnetic behaviour

TABLE-3
MAGNETIC PROPERTIES OF Mg-Zn FERRITE NANOPARTICLES WITH VARYING COMPOSITIONS

Samples	Sample code	Magnetization (M_s) (emu/g)	Remanent magnetization (M_r) (emu/g)	Coercivity (H_c) (Oe)	Squareness ratio (M_r/M_s)
$MgFe_2O_4$	S1	12.54	2.79	111.15	0.22
$Mg_{0.75}Zn_{0.25}Fe_2O_4$	S2	4.07	0.09	183.49	0.02
$Mg_{0.5}Zn_{0.5}Fe_2O_4$	S3	28.53	2.14	49.88	0.07
$Mg_{0.25}Zn_{0.75}Fe_2O_4$	S4	10.33	0.61	48.71	0.06
$ZnFe_2O_4$	S5	6.18	0.05	67.46	0.01

2.14 emu/g, further demonstrating its exceptional magnetic properties (Table-3).

From $MgFe_2O_4$ to $ZnFe_2O_4$, the coercivity (H_c) values decreased as the Zn substitution increased. Due to enhanced anisotropy contributions from Mg-rich locations, $Mg_{0.75}Zn_{0.25}Fe_2O_4$ (183.49 Oe) exhibited the maximum coercivity, whereas $Mg_{0.25}Zn_{0.75}Fe_2O_4$ (48.71 Oe) exhibited the lowest. The magnetic anisotropy is reduced with increasing Zn concentrations, which is in line with the soft magnetic properties of ferrites that are rich in Zn [22]. Among the samples tested, $MgFe_2O_4$ had the greatest squareness ratio (M_r/M_s), indicating that a considerable portion of the sample's magnetization was preserved even after the applied field was removed.

The magnetic behaviour and blocking temperature (TB) of the synthesized spinel ferrite samples gave better understand by examining the zero field cooled (ZFC) and field cooled (FC) magnetization curves (Fig. 6). Once the samples were brought to low temperatures without a magnetic field, we heated them with one and employed it to generate the ZFC curves. On the other hand, FC curves were determined by subjecting samples to a cooling process while a field was applied. At the blocking temperature, a distinctive peak appears in the ZFC curves of all samples, signifying the passage from the blocked to the superparamagnetic state. In contrast, the FC curves demonstrated that aligned spins induced by the applied field continue to expand or attain saturation at lower temperatures and lacked a distinct peak.

A relatively high blocking temperature, a clean separation of the FC and ZFC curves and a progressive fall in the ZFC curve are all characteristics of the $MgFe_2O_4$ sample. Anisotropy energy and modest interparticle interactions are suggested by this behaviour. Lower blocking temperatures and larger peaks are seen in the ZFC curves of the mixed Mg-Zn ferrites. Since the replacement of Zn reduces the magneto-crystalline anisotropy, this indicates that the energy of magnetic anisotropy has decreased. Among the samples in the series, sample $Mg_{0.5}Zn_{0.5}Fe_2O_4$ shows the highest saturation magnetization, in agreement with the M-H findings. The large ZFC peak suggests a variety of particle sizes and anisotropy energies, whereas the abrupt rise in the FC curve at low temperatures implies significant spin alignment. There is little distinction between the ZFC and FC curves and the lowest blocking temperature for the Zn-rich sample $ZnFe_2O_4$. Because of the low spin alignment and non-interacting particles, this indicates weak anisotropy energy and superparamagnetic behaviour. The magnetic characteristics, such as magnetization values and anisotropy constants, obtained from the M-H loops agreed with the patterns shown in the ZFC and FC data. As these studies illustrate, magnetic characteristics are significantly influenced by particle size, composition, and inter-particle interactions. The presence of Zn diminishes anisotropy energy, while Mg substitution preserves ferrimagnetic characteristics, leading to a balanced behaviour of the material between two extremes.

Antimicrobial activity: The synthesized ferrite samples *viz*. $MgFe_2O_4$, $Mg_{0.75}Zn_{0.25}Fe_2O_4$, $Mg_{0.5}Zn_{0.5}Fe_2O_4$, $Mg_{0.25}Zn_{0.75}Fe_2O_4$ and $ZnFe_2O_4$ were tested against Gram-positive bacteria (*Staphylococcus aureus*) and fungi (*Candida albicans*) to determine their antibacterial and antifungal properties. At a concentration of 100 µL, the antibacterial activity of $Mg_{0.25}Zn_{0.75}Fe_2O_4$ and $ZnFe_2O_4$ against *Staphylococcus aureus* was the highest, with a zone of inhibition (ZOI) of 3 mm (Table-4). This is notably lower than the ZOI of 14 mm displayed by the standard anti-

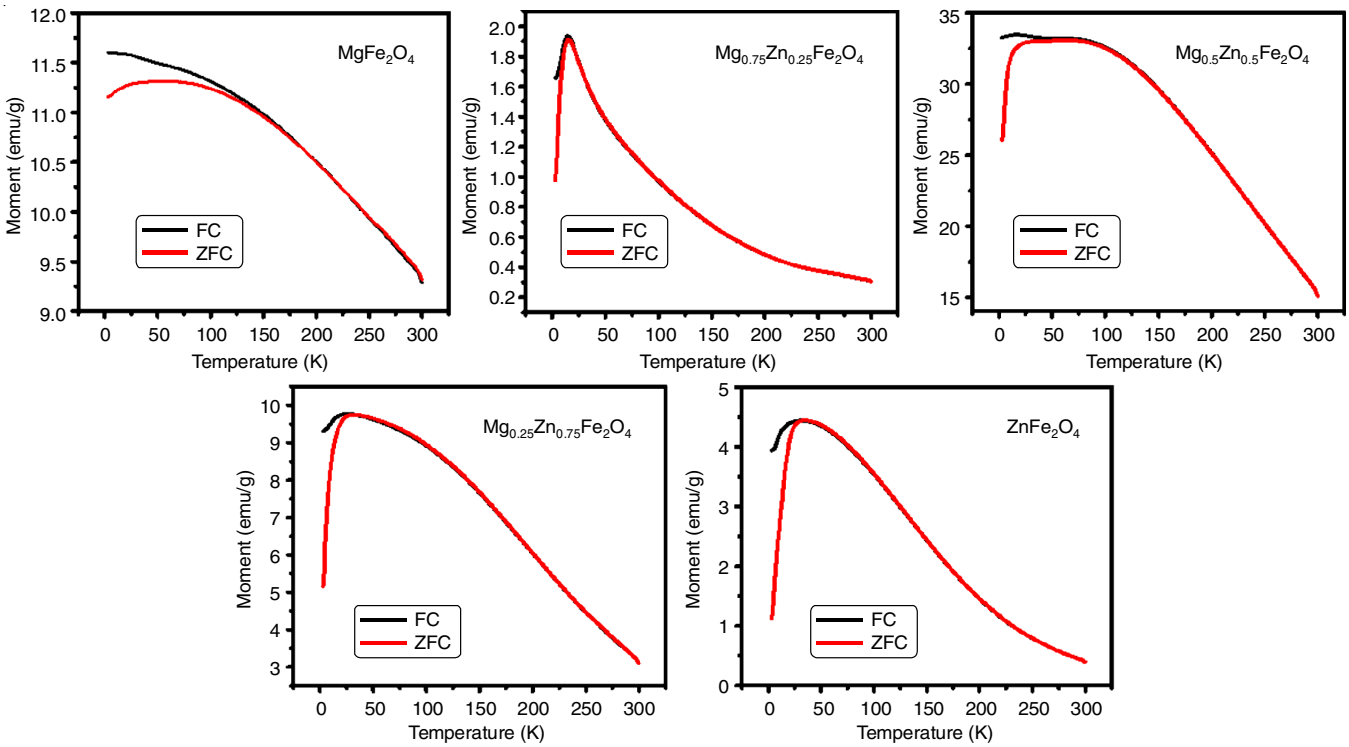

Fig. 6. Field-cooled (FC) and zero-field-cooled (ZFC) magnetization curves for Mg-Zn ferrite nanoparticles ($MgFe_2O_4$, $Zn_{0.25}Mg_{0.75}Fe_2O_4$, $Zn_{0.5}Mg_{0.5}Fe_2O_4$, $Zn_{0.75}Mg_{0.25}Fe_2O_4$ and $ZnFe_2O_4$), showing temperature-dependent magnetic behaviour

TABLE-4
ANTIMICROBIAL ACTIVITY DATA OF Mg-Zn FERRITE NANOPARTICLES SHOWING INHIBITION ZONE DIAMETERS (mm) COMPARED TO STANDARD CONTROLS

Sample	*Staphylococcus aureus*	*Candida albicans*
$MgFe_2O_4$	–	3
$Mg_{0.75}Zn_{0.25}Fe_2O_4$	2	2
$Mg_{0.5}Zn_{0.5}Fe_2O_4$	2	–
$Mg_{0.25}Zn_{0.75}Fe_2O_4$	3	1
$ZnFe_2O_4$	3	2
Standard	14	8

biotic. In comparison to the typical antifungal drug, which demonstrated a zone of inhibition (ZOI) of 8 mm, $MgFe_2O_4$ exhibited antifungal activity against *Candida albicans*, achieving a ZOI of 3 mm at a concentration of 25 µL as shown in Table-5. Depending on the microbiological strain and concentration, other samples, including $Mg_{0.75}Zn_{0.25}Fe_2O_4$ and $Mg_{0.5}Zn_{0.5}Fe_2O_4$, displayed modest antibacterial and antifungal activities, with ZOIs ranging from 1 to 2 mm (Table-6).

A tendency towards enhanced antibacterial action, especially against Gram-positive bacteria, was observed in the comparative study as the zinc level in the ferrite lattice increased. The effect of Zn^{2+} ionic radius and electrochemical characteristics on the surface interface between nanoparticles and bacterial cells is responsible for this improvement. In $Mg_{0.25}Zn_{0.75}Fe_2O_4$ and $ZnFe_2O_4$, for example, zinc replaces magnesium. This results in smaller particles and more release of Zn^{2+} ions, which can damage microbial cell membranes and alter internal enzyme pathways. The inclusion of magnesium in $MgFe_2O_4$ causes oxidative stress by producing reactive oxygen species (ROS), which explains its antifungal effect. The results are supported by the MIC data, which demonstrate that at concentrations of 25 µL, $MgFe_2O_4$ and $Mg_{0.75}Zn_{0.25}Fe_2O_4$ efficiently eliminate *Candida albicans*. On the other hand, greater concentrations were required for $Mg_{0.5}Zn_{0.5}Fe_2O_4$, $Mg_{0.25}Zn_{0.75}Fe_2O_4$ and $ZnFe_2O_4$ to achieve the same results.

The antibacterial activity of these ferrites is likely due to a complex process involving many routes. To begin, the microbial cell membranes are disrupted when the positively charged ferrite nanoparticles come into contact with their negatively charged counterparts. Additionally, the release of metal ions like Zn^{2+} and Mg^{2+} disrupts the metabolic activities of microbes. Thirdly, the oxidative damage to DNA, proteins and lipids in microbes is caused by the ROS generated by the nanoparticles. Previous studies [23,24] indicate that Mg-Zn ferrites exhibit greater activity compared to pure Mg or Zn ferrites, and this synergistic effect of ion release and reactive oxygen species production aligns with these findings. The results indicated that $ZnFe_2O_4$ and $Mg_{0.25}Zn_{0.75}Fe_2O_4$ are the most promising Mg-Zn ferrite nanoparticles for the development of new antibacterial agents that can target bacteria and viruses that are resistant to drugs.

Zeta potential: Samples zeta potential data is shown in Table-7. An examination of the relationship between zeta potential and antibacterial activity reveals the close relationship between surface charge characteristics and biological effectiveness. The influence of surface charges on the interactions between Mg-Zn ferrite nanoparticles and microbial membranes can be inferred from their zeta potential values. In terms of antibacterial activity against *Staphylococcus aureus* and *Candida albicans* species, samples with larger negative zeta potentials, such $Mg_{0.5}Zn_{0.5}Fe_2O_4$ (-9.90 mV) and $Mg_{0.25}Zn_{0.75}Fe_2O_4$ (-7.35 mV), are preferred. The negative charge on the surface enhances its electrostatic attraction to positively charged microbial membranes, leading to membrane disruption and increased effectiveness in inhibiting bacteria [23,24].

$Mg_{0.25}Zn_{0.75}Fe_2O_4$ and $ZnFe_2O_4$, which have intermediate zeta potentials of -7.35 mV and -2.17 mV, respectively, show better antibacterial activity against fungi and Gram-positive bacteria. This finding provides more evidence that their antibacterial action is due to mechanisms other than surface charge, such as the release of ions (Zn^{2+} and Mg^{2+}) and the formation of reactive oxygen species (ROS). As an example, the increased

TABLE-5
MINIMUM INHIBITORY CONCENTRATION (MIC) DATA (mm) OF Mg-Zn FERRITE NANOPARTICLES AT DIFFERENT CONCENTRATIONS

Sample ID	Minimum inhibitory concentration (mm)				MIC of sample (µL)
	25 µL	50 µL	75 µL	100 µL	
$MgFe_2O_4$	–	–	–	–	–
$Mg_{0.75}Zn_{0.25}Fe_2O_4$	–	–	2	4	75
$Mg_{0.5}Zn_{0.5}Fe_2O_4$	–	–	1	3	100
$Mg_{0.25}Zn_{0.75}Fe_2O_4$	–	–	–	3	100
$ZnFe_2O_4$	–	–	–	–	–

TABLE-6
MINIMUM INHIBITORY CONCENTRATION (MIC) DATA (mm) OF Mg-Zn FERRITE NANOPARTICLES AT DIFFERENT CONCENTRATIONS

Sample ID	Minimum inhibitory concentration (mm)				MIC of sample (µL)
	25 µL	50 µL	75 µL	100 µL	
$MgFe_2O_4$	3	5	7	9	25
$Mg_{0.75}Zn_{0.25}Fe_2O_4$	2	3	4	5	25
$Mg_{0.5}Zn_{0.5}Fe_2O_4$	–	–	–	–	–
$Mg_{0.25}Zn_{0.75}Fe_2O_4$	–	1	2	3	50
$ZnFe_2O_4$	–	2	4	5	50

TABLE-7
ZETA POTENTIAL, MOBILITY AND ELECTRIC FIELD (E. Field) VALUES OF Mg-Zn FERRITE NANOPARTICLES

Sample	Zeta potential (mV)	Mobility (cm^2/Vs)	E. Field (V/cm)
$MgFe_2O_4$	-3.10	-2.417×10^{-5}	-16.20
$Mg_{0.75}Zn_{0.25}Fe_2O_4$	-4.07	-3.174×10^{-5}	-16.24
$Mg_{0.5}Zn_{0.5}Fe_2O_4$	-9.90	-7.717×10^{-5}	-16.19
$Mg_{0.25}Zn_{0.75}Fe_2O_4$	-7.35	-5.735×10^{-5}	-16.26
$ZnFe_2O_4$	-2.17	-1.691×10^{-5}	-16.29

surface contact and Zn content of $Mg_{0.25}Zn_{0.75}Fe_2O_4$ are consistent with its minimum inhibitory concentration (MIC) of 100 µL for *Staphylococcus aureus* and *Candida albicans*.

The antibacterial capabilities of spinel ferrite nanoparticles have been associated with their capacity to produce reactive oxygen species (ROS) and release metal ions, which is in line with our results. Their adhesion to microbial membranes is further modulated by the zeta potential, which facilitates their mode of action. The findings highlighted the significance of enhancing surface and structural features for use in biomedicine, especially in the fight against drug-resistant microbes.

Conclusion

The outstanding structural, magnetic and antibacterial capabilities of the synthesized Mg-Zn ferrite nanoparticles were driven by their adjustable composition and surface charge. Spinel ferrites were successfully formed with lattice characteristics affected by Zn substitution, resulting in a decrease in a crystallite size from 36.6 nm ($MgFe_2O_4$) to 22.17 nm ($ZnFe_2O_4$), as validated by XRD and Raman spectroscopic studies. The magnetic properties of Mg-Zn compositions showed that there was a wide range of saturation magnetization (12.54 to 28.53 emu/g), coercivity (111.15 to 49.88 Oe) and anisotropy constant (2.506×10^5 to 0.382×10^5 J/m^3), which might be used for energy storage. Due to increased ion release and ROS formation, Zn-rich samples, including $ZnFe_2O_4$, showed better antibacterial activity, with inhibition zones of up to 3 mm against Gram-positive bacteria. The significance of surface charge in microbial contacts was brought to light by zeta potential data, which demonstrated that $Mg_{0.5}Zn_{0.5}Fe_2O_4$ (-9.90 mV) exhibited improved electrostatic interactions. Thus, these results highlighted the multipurpose nature of Mg-Zn ferrites, which bodes well for their potential use in energy storage, magnetic devices and antibacterial therapies.

ACKNOWLEDGEMENTS

The authors would like to extend their heartfelt gratitude to Chaitanya Bharathi Institute of Technology (CBIT), Hyderabad, India, for their generous funding and unwavering support under the faculty and student research projects. This support was provided under sanction order no. CBIT/PROJ-IH/1013/Chemistry/0001/2024, CBIT/PROJ-SIH/I002/Chemistry/D001/2024 and CBIT/PROJSIH/I003/Chemistry/D002/2024, dated 26 March, 2024.

CONFLICT OF INTEREST

The authors declare that there is no conflict of interests regarding the publication of this article.

REFERENCES

1. S.J. Salih and W.M. Mahmood, *Heliyon*, **9**, e16601 (2023); https://doi.org/10.1016/j.heliyon.2023.e16601
2. Y. Zhang, X. Feng, Z. Zheng, Z. Zhang, K. Lin, X. Sun, G. Wang, J. Wang, J. Wei, P. Vallobra, Y. He, Z. Wang, L. Chen, K. Zhang, Y. Xu and W. Zhao, *Appl. Phys. Rev.*, **10**, 011301 (2023); https://doi.org/10.1063/5.0104618
3. K.R. Sanchez-Lievanos, J.L. Stair and K.E. Knowles, *Inorg. Chem.*, **60**, 4291 (2021); https://doi.org/10.1021/acs.inorgchem.1c00040
4. D. Carta, M.F. Casula, A. Falqui, G. Mountjoy, C. Sangregorio, D. Loche and A. Corrias, *J. Phys. Chem. C*, **113**, 8606 (2009); https://doi.org/10.1021/jp901077c
5. M. Ramazanov, A. Karimova and H. Shirinova, *Biointerf. Res. Appl. Chem.*, **11**, 8654 (2020); https://doi.org/10.33263/BRIAC112.86548668
6. N. Matsubara, T. Masese, E. Suard, O.K. Forslund, E. Nocerino, R. Palm, Z. Guguchia, D. Andreica, A. Hardut, M. Ishikado, K. Papadopoulos, Y. Sassa and M. Månsson, *Inorg. Chem.*, **59**, 17970 (2020); https://doi.org/10.1021/acs.inorgchem.0c02241
7. H.L. Andersen, C. Granados-Miralles, K.M.Ø. Jensen and M. Saura-Múzquiz and M. Christensen, *ACS Nano*, **18**, 9852 (2024); https://doi.org/10.1021/acsnano.3c08772
8. N. Torres-Gómez, O. Nava, L. Argueta-Figueroa, R. García-Contreras, A. Baeza-Barrera and A.R. Vilchis-Nestor, *J. Nanomater.*, **2019**, 7921273 (2019); https://doi.org/10.1155/2019/7921273
9. N. Yahya, A.S.M. Aripin, A.A. Aziz, H. Daud, H.M. Zaid, L.K. Pah and N. Maarof, *Am. J. Eng. Appl. Sci.*, **1**, 53 (2008); https://doi.org/10.3844/ajeassp.2008.53.56
10. A. Rabbani, R. Haghniaz, T. Khan, R. Khan, A. Khalid, S.S. Naz, M. Ul-Islam, F. Vajhadin and F. Wahid, *RSC Adv.*, **11**, 1773 (2021); https://doi.org/10.1039/D0RA08417D
11. K.K. Kefeni, T.A.M. Msagati, T.TI. Nkambule and B.B. Mamba, *Mater. Sci. Eng. C*, **107**, 110314 (2020); https://doi.org/10.1016/j.msec.2019.110314
12. A.A. Abdelrahman, A.S.A. Raboh, M.M. Ismail, H.H. El-Bahnasawy and D.A. Rayan, *Appl. Phys. A*, **130**, 682 (2024); https://doi.org/10.1007/s00339-024-07794-z
13. M.E. Hiti, A.I.E. Shora and S.M. Hammad, *Mater. Sci. Technol.*, **13**, 625 (1997); https://doi.org/10.1179/mst.1997.13.8.625
14. A. Henaish, *Arab J. Nuclear Sci. Appl.*, **0**, 0 (2019); https://doi.org/10.21608/ajnsa.2019.11102.1195
15. M.A. Darwish, M.M. Hussein, S.A. Saafan, W. Abd-Elaziem, D. Zhou, M.V. Silibin, S.V. Trukhanov, N.V. Abmiotka, M.I. Sayyed, D.I. Tishkevich and A.V. Trukhanov, *J. Alloys Compd.*, **968**, 172278 (2023); https://doi.org/10.1016/j.jallcom.2023.172278
16. K.A. Khalaf, *Adv. Mater.*, **8**, 70 (2019); https://doi.org/10.11648/j.am.20190802.15
17. H. Saqib, S. Rahman, R. Susilo, B. Chen and N. Dai, *AIP Adv.*, **9**, 055306 (2019); https://doi.org/10.1063/1.5093221
18. A.M. Padhan, S. Nayak, M. Sahu, Z. Jaglièic, P. Ko•elj and H.J. Kim, *Physica B*, **668**, 415245 (2023); https://doi.org/10.1016/j.physb.2023.415245
19. P. Kumar, J. Asokan, S. Sriram, M.C. Ramkumar, P.S. Kumar and M.G. Shalini, *J. Hazard. Mater. Adv.*, **17**, 100594 (2025); https://doi.org/10.1016/j.hazadv.2025.100594
20. C.A. Palacio Gómez, C.A. Barrero Meneses and J.A. Jaén, *J. Magn. Magn. Mater.*, **505**, 166710 (2020); https://doi.org/10.1016/j.jmmm.2020.166710
21. B.K. Ostafijchuk, V.S. Bushkova, V.V. Moklyak and R.V. Lnitsky, *Ukrainian J. Phys.*, **60**, 1234 (2015); https://doi.org/10.15407/ujpe60.12.1234
22. A. Ghosh, M. Satalkar, S. Rathod, S.P. Nag, P. Vyas, N. Kane, N. Ghodke, R. Prasad and R. Dwivedi, *Int. J. Mod. Phys. Conf. Ser.*, **22**, 28 (2013); https://doi.org/10.1142/S2010194513009896
23. B. Gottenbos, D.W. Grijpma, H.C. Van Der Mei, J. Feijen and H.J. Busscher, *J. Antimicrob. Chemother.*, **48**, 7 (2001); https://doi.org/10.1093/jac/48.1.7
24. R. Kügler, O. Bouloussa and F. Rondelez, *Microbiology*, **151**, 1341 (2005); https://doi.org/10.1099/mic.0.27526-0